



Temperature-Dependent Variations in Structural, Magnetic, and Optical Behavior of Doped Ferrites Nanoparticles

M. Saqib¹ · S. S. Ali^{1,2} · M. Zulqarnain¹ · Muhammad U. Qadri¹ · M. Riaz³ · M. S. Hasan¹ · M. I. Khan¹ · M. Tahir^{1,4} · M. I. Arshad⁵ · H. S. Rani¹

Received: 19 July 2020 / Accepted: 26 October 2020 / Published online: 7 November 2020
© Springer Science+Business Media, LLC, part of Springer Nature 2020

Abstract

Nanocrystalline Mn-Zn ferrite nanopowders ($Mn_{0.5}Zn_{0.5}Fe_2O_4$) were synthesized by co-precipitation technique and post-fabrication annealing has been performed at different temperature ranges from 400 to 700 °C for 2 h. The effect of annealing on morphology, crystalline phase formation, cation distribution, lattice constant, particle size, magnetic properties, and optical properties was studied by scanning electron microscopy (SEM), x-ray diffraction (XRD), vibrating sample magnetometer (VSM), and UV-visible spectroscopy (UV-Vis) respectively. The crystallite size increased from 14 to 24 nm with the annealing temperature owing to the grain growth process or more technically we say Ostwald ripening mechanism. The decomposition of ferrites at low-temperature results in the formation of hematite Fe_2O_3 eventually reduced the magnetic properties of ferrites. The hematite, impurity phase, started to dissolve or converted into the ferrite phase after 600 °C. The sample annealed at 700 °C shows a better crystalline structure, phase formation, and larger magnetization compared to the other ferrite samples. The improved magnetic behavior after heat treatment is due to the better alignment of domains at the cost of the grain growth process. The UV-Vis spectroscopy result revealed the maximum absorbance at 380 nm.

Keywords Annealing · Nanostructures · Magnetic properties · Optical properties

1 Introduction

The nanocrystalline ferrites have gained much attention due to their technological applications. Scientists are keen to investigate the various properties of doped ferrites prepared by different methods. The soft spinel ferrites are the most important class because of their technological application [1–4] since Mn-Zn

ferrites belong to the direct band gap materials so they can be used for optoelectronic sources. While dealing with the spinel ferrites, in the general formula, MFe_2O_4 M represents the divalent metal cations like Mn^{2+} , Zn^{2+} , Co^{2+} , and Ni^{2+} . The divalent metal cations having ionic radii greater than 1 Å cannot form the spinel structure [5, 6]. Tetrahedral and octahedral are the two interstitial sites occupied by the metal cations present in the spinel geometry. The distribution of metal cations between the two sites is responsible for the formation of any of three types of spinel, normal, inverse, and mixed spinels. The concentrations of cations between the two sites highly influence the structural and magnetic properties of ferrites [7–9].

The magnetic properties of spinel structures are often tuned owing to the non-magnetic cations when they are introduced interstitially or as a replacement to host material's atoms [10]. For instance, zinc ferrites can be doped with Mg^{2+} ions which significantly change the magnetic behavior; in fact, it can increase the saturation magnetization and other relevant parameters [11]. Furthermore, the core-shell structures comprising of agglomerated Zn-Mg-Fe microspheres have been prepared through solvothermal technique and investigated as photocatalysts in the degradation of 1,2-dichlorobenzene

✉ S. S. Ali
ssa_pu@hotmail.com

¹ Department of Physics, The University of Lahore, Lahore 54000, Pakistan

² School of Physical Sciences, University of the Punjab, Lahore 54590, Pakistan

³ Department of Physics, University of the Punjab, Lahore 54590, Pakistan

⁴ Department of Applied Chemistry, School of Science, Xi'an Jiaotong University, Xi'an 710049, China

⁵ Department of Physics, Government College University, Faisalabad 38000, Pakistan

[12–17]. In the wet chemical method, co-precipitation provides homogenous and smaller crystallite size as compared to the other preparation techniques that involve the solid-state reaction and high temperature. In this paper, Mn-Zn ferrites are prepared by the co-precipitation method. The as-synthesized sample was annealed at 400 °C, 500 °C, 600 °C, and 700 °C for 2 h each. In the formation of oxides or spinels, the choice of the precursor is very important. Morphological, structural, magnetic, and optical properties were investigated.

2 Experimental

Mn_{0.5}Zn_{0.5}Fe₂O₄ powder was synthesized through the co-precipitation method. MnCl₂·6H₂O, ZnCl₂·6H₂O, and FeCl₂·4H₂O were used as starting materials. To get the desired stoichiometry, we prepared 50 ml solution of MnCl₂·6H₂O, 50 ml solution of ZnCl₂·6H₂O, and 100 ml solution of FeCl₂·4H₂O in the de-ionized water and mixed thoroughly at 80 °C. The separate solution of 0.8 M NaOH has been prepared and mixed drop wise as the precipitating agent. The solutions were homogeneously mixed on the magnetic stirrer while the precipitating agent was added to the solution to maintain the desired pH around 12. Homogeneous mixing is very important otherwise separation of phase can take place. The reaction was continued for 60–70 min at a temperature of 80 °C under constant stirring. The metal salts converted into hydroxide and then to nano-ferrites upon heating to 80 °C for 60 min. Thus, reaction time was enough for the transformation of metal hydroxide into the spinel ferrite phase. The precipitates got stable at the bottom of the vessel since they are less soluble in the remaining solution. After the completion of the reaction, the reaction vessel has been taken to room temperature and the precipitates were separated from the rest of the solution. These precipitates were washed 5 to 6 times with distilled water and 3 to 4 times with ethanol in order to remove the impurities. After washing, the precipitates were placed inside the drying oven at 80 °C for 4 h in order to remove the excess water. The dried product was then very smoothly crushed with the help of mortar and pestle into powder form. All the steps are clearly illustrated schematically in Fig. 1 as shown below.

The final product was annealed at 400 °C, 500 °C, 600 °C, and 700 °C in the annealing chamber for 2 h each. X-ray diffraction (XRD-Philips/PANalytical X'Pert Pro-MPD) analysis was performed to study the crystal structure, phase formation, and crystallite size of as-synthesized and annealed samples. The morphological and elemental analysis was done by using a scanning electron microscope (TESCAN Vega LMU Variable Pressure SEM) and EDX analyses. A vibrating sample magnetometer (VSM-7407, Lakeshore) has been employed to study the magnetic behavior of samples and to observe the possible change in magnetic parameters owing to

the heat treatment. The optical properties of ferrites were investigated by UV-Visible spectrophotometer (Perkin Elmer Lambda 25).

3 Results and Discussion

Mn_{0.5}Zn_{0.5}Fe₂O₄ as-synthesized and annealed at 400 °C, 500 °C, 600 °C, and 700 °C for 2 h each has been investigated for its structural properties as shown in Fig. 2. These diffraction peaks are well matched with JCPDS card no. 10-0467 confirming the formation of Mn-Zn ferrites in all samples [18]. The diffraction peaks corresponding to spinel ferrites (220), (311), (422), (511), and (440) are indexed in accordance with the JCPDS card as mentioned above. The diffraction peaks belong to hematite are indicated with an asterisk with the help of JCPDS card no. 33-0664 [19]. The as-prepared sample shows only three minor peaks at angle 30°, 35.3°, and 62.2° so in order to get the better crystalline structure and more diffraction peaks at various angles annealing have been employed for 2 h with a stepwise increase in temperature from 400 to 700 °C. After the heat treatment, sharper peaks can be observed in the figure owing to the release of stress in the unit cell. This happens due to the removal of contaminations in the sample and unnecessary contents present in the freshly prepared samples.

The lattice parameter has been calculated as

$$a = d\sqrt{h^2 + k^2 + l^2}$$

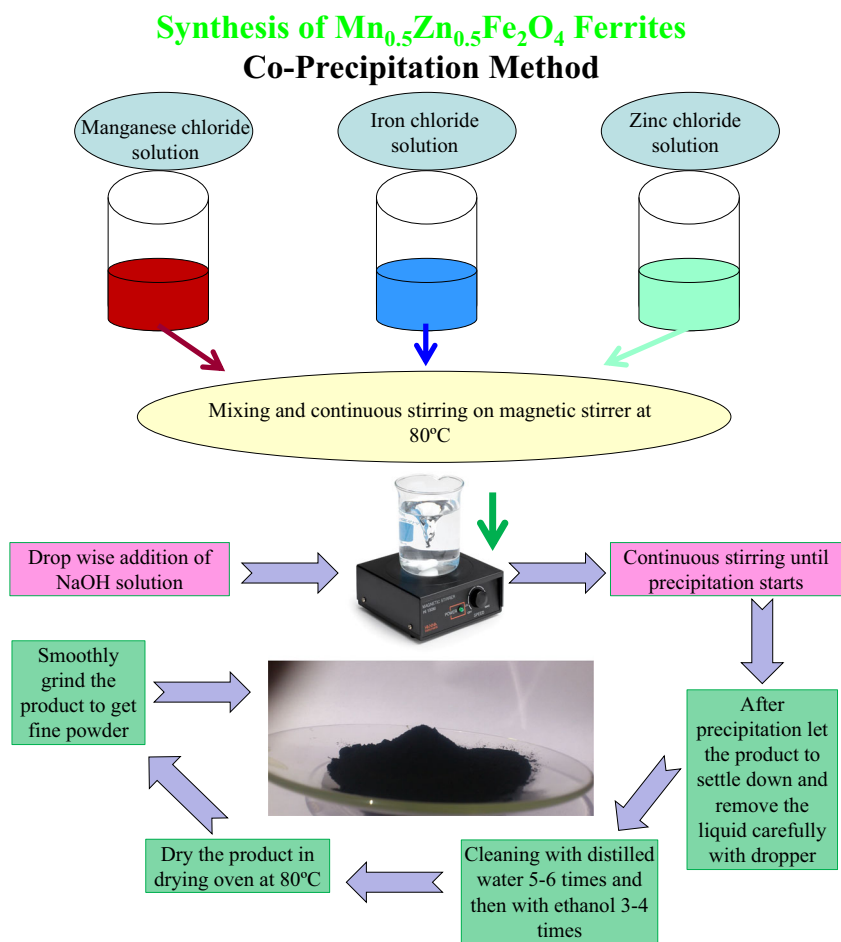
Considering all the planes as shown in Fig. 2, the calculated average value of unit cell edge length is 8.42 Å. This value is in agreement with the already reported values in the literature. The average crystallite size of different peaks has been calculated by using Scherrer's relation [20].

$$D = \frac{0.89 \lambda}{\beta \cos \theta}$$

D shows average crystallite dimension, 0.89 is shape factor, $\lambda = 0.154$ nm, and β is linked with peak broadening, i.e., FWHM. The peak broadening is affected by many factors such as stress, strain, deformation, and size. The broadening due to size and strain must be taken into account for the calculation of grain size. Commonly, the broadening of XRD peaks is associated with the reduction of crystallite size [21].

Figure 3 shows the graph between annealing temperature and average particle size for all samples illustrating a gradually increasing particle size with temperature. The grain size, crystal growth, and crystallization are highly affected by the annealing temperature. Normally, grain size increases with an increase of annealing temperature. This may be explained by the nucleation and growth of particles in a solid solution, as the two are the process of crystallization. In the heating

Fig. 1 Complete co-precipitation synthesis process illustrated schematically



process, when the particles are formed, they collide and either coalesce with one another to form a larger particle or coagulate. This is pretty straightforward crystal growth. Annealing any solid-state crystalline material to sufficient temperatures

will enable Oswald ripening, i.e., larger grains grow bigger at the expense of smaller grains. The rate-limiting factors are diffusion oriented. Hence, grain growth typically goes exponentially with temperature, only linearly with time at a given

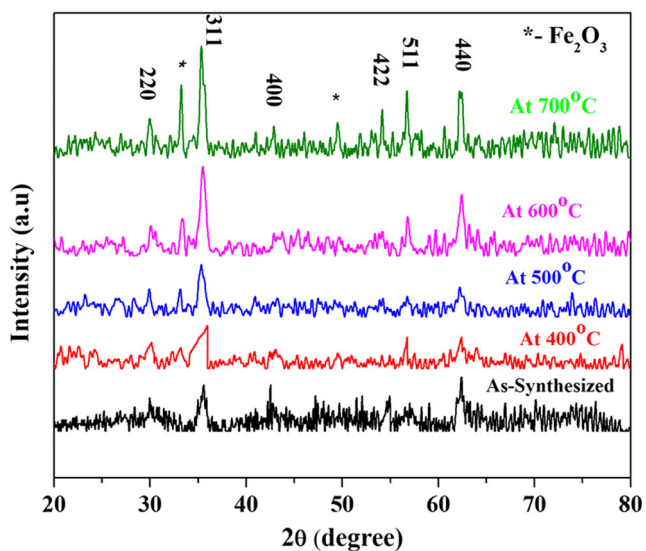


Fig. 2 XRD patterns of $Mn_{0.5}Zn_{0.5}Fe_2O_4$ ferrites nanoparticles annealed at different temperatures for 2 h

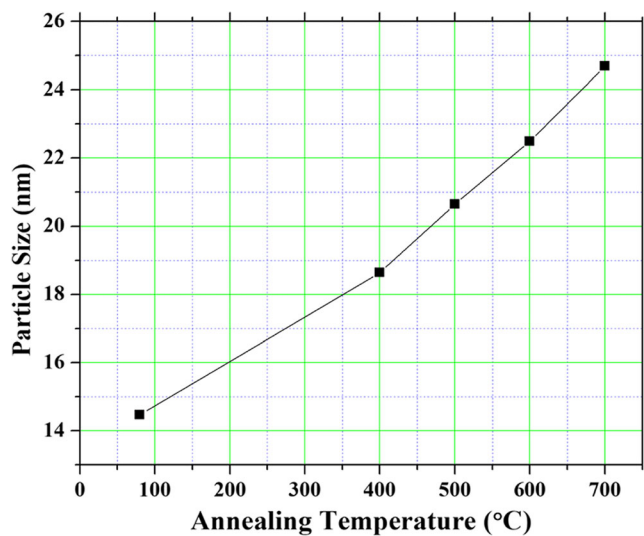
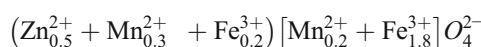


Fig. 3 Variation in particle size with the increase in annealing temperature

temperature. The average crystallite size for all the samples is in the range of 14–24 nm. It is inferred from the results that the co-precipitation method yields a smaller crystallite size of Mn-Zn ferrites than the other reported methods [22]. The reason behind Ostwald ripening is that Ostwald ripening is basically a function of the surface area to volume ratio. In a given sample, crystallites are in a range in size from very small to very large. The smallest crystallites have the largest surface area to volume ratio. Given their higher surface area, it is more likely they will dissolve (melt) as the temperature is increased. This dissolved (or melted) mass then gradually deposits on the crystals that remain, which were already larger to begin with. The larger crystals grow larger at the expense of the small crystals getting smaller (or disappearing altogether). The temperature simply increases the rate at which this phenomenon occurs [23]. The physical behavior of ferrites is highly influenced by the dopants category, annealing temperature, and cation distribution between the two sites, A and B. Oxygen ions determine the crystal structure since the radii of oxygen ion is much larger than metal ion, Mn and Zn. The cation distribution is influenced by the synthesis method and annealing temperature [24].

The ionic radii, electronic configuration, and electrostatic energy affect the distribution of metal ions over the two sites. In the account of electronic configuration, Zn^{2+} has filled d-shell orbital and hence shows a tendency to occupy the tetrahedral site. This may be attributed to the formation of sp^3 hybrid orbital [4]. In addition to it, if we take into account the crystal field stabilization energy for a transition metal, the zinc shows excess energy stabilization for the tetrahedral site [25]. While the Fe^{3+} and Mn^{2+} are distributed over the two sites, tetrahedral and octahedral. Hence, the cation distribution for the $Mn_{0.5}Zn_{0.5}Fe_2O_4$ can be written as.



where () and [] brackets represent the tetrahedral and octahedral sites respectively. The experimental lattice parameter calculated from the X-ray diffraction data increases to some extent with the annealing temperature. The theoretical lattice parameter a_{th} was calculated for the correlation between ionic radii and to check the proposed cation distribution from the following relation.

$$a_{th} = \frac{8}{3\sqrt{3}} \left[(r_A + R_O) + \sqrt{3} (r_B + R_O) \right]$$

where R_o is the radius of oxygen ion and 1.38 Å, r_A and r_B are the ionic radii of the tetrahedral and octahedral sites and can be calculated by knowing the cation distribution. The theoretical parameter a_{th} calculated from relation is 8.44 Å. The theoretical and experimental lattice parameters are in good agreement confirming the cation distribution.

The ionic radii of each site were calculated according to the following relation

$$r_A = [(0.5)r_{Zn}^{2+} + (0.3)r_{Mn}^{2+} + (0.2)r_{Fe}^{3+}]$$

$$r_B = 0.5 [(0.2)r_{Mn}^{2+} + (1.8)r_{Fe}^{3+}]$$

where r_{Zn}^{2+} , r_{Mn}^{2+} , and r_{Fe}^{3+} are ionic radii of the Zn^{2+} , Mn^{2+} , and Fe^{3+} ions respectively.

The oxygen parameter which is quite important in the case of spinels has been calculated from the following relation.

$$u = \left[(r_A + R_O) \frac{1}{a\sqrt{3}} + \frac{1}{4} \right]$$

The value of the oxygen parameter was calculated by 0.391 Å by using the value of the tetrahedral site radius, radius of oxygen ion, and experimentally calculated lattice parameter in the above relation. The value of the oxygen parameter is 0.375 Å in the case of ideal spinels having exactly cubic closed packing. The value of the oxygen parameter obtained from the above relation is slightly larger than the ideal value which is probably due to the small displacement of ion along the body diagonal due to the expansion of the tetrahedral site. The large concentration of Zn^{2+} having larger ionic radii 0.68 Å as compared to the Fe^{3+} , 0.58 Å, leads to the slight variation in the ideal position of oxygen anions. The change in the experimentally calculated lattice parameter is also confirmed by this lattice disturbance [26]. The proposed increase in oxygen parameter u reveals the trigonal distortion at the octahedral B site. The proposed cation distribution in the two sites and resulting lattice expansion has been further checked by calculating the tetrahedral bond length, octahedral bond length, tetrahedral shared edge, octahedral shared edge, and unshared site edges (d_{AO} , d_{BO} , d_{AE} , d_{BE} , and d_{BEU} respectively) of spinel lattice by using the value of theoretically calculated lattice constant and oxygen parameter from the following relations [23].

$$d_{AO} = a\sqrt{3}(u-0.25)$$

$$d_{BO} = a \left(\sqrt[3]{3u^2 - \frac{11}{4}u + \frac{43}{64}} \right)$$

$$d_{AE} = a\sqrt{2}(2u-0.5)$$

$$d_{BE} = a\sqrt{2}(1-2u)$$

$$d_{BEU} = a\sqrt[3]{4u^2 - 3u + \frac{11}{16}}$$

$$L_A = a \frac{\sqrt[3]{3}}{4}$$

$$L_B = a \frac{\sqrt[3]{2}}{4}$$

L_A and L_B are the hopping lengths. The obtained values are listed in Table 1 where the larger values of d_{AO} , d_{BO} , d_{AE} , d_{BE} , d_{BEU} , L_A , and L_B are attributed to the larger concentration of Mn ions and cation distribution.

Table 1 The bond length of A site d_{AO} and B site d_{BO} , the tetrahedral edge d_{AE} , the shared and unshared octahedral edges d_{BE} and d_{BEU} , and hopping length at A site L_A and B site L_B for $Mn_{0.5}Zn_{0.5}Fe_2O_4$

x	d_{AO}	d_{BO}	d_{AE}	d_{BE}	d_{BEU}	L_A	L_B
0.5	2.060 Å	1.951 Å	3.315 Å	2.58 Å	2.96 Å	3.612 Å	2.965 Å

The morphology of nanocrystalline $Mn_{0.5}Zn_{0.5}Fe_2O_4$ has been studied by scanning electron microscopy. The direct observation of the micrographs reveals that the morphology is porous and agglomerated. The segregation of the particles may be due to the magnetic behavior of the transition metals [5]. The small black voids representing the pores in the prepared ferrites [26]. The SEM micrographs of the as-synthesized sample are shown in Fig. 4 with different magnifications. The annealing temperature has the predominant effect on the formation of clear crystalline structure and homogeneous microstructure which is already elaborated through XRD analysis.

The compositional analysis was done by the EDX analysis as shown Fig. 5. The EDX spectrum indicates the presence of Mn, Zn, Fe, and O which confirms the formation of Mn-Zn ferrites.

The M-H hysteresis loops of as-synthesized and annealed samples have been measured by employing VSM as shown in Fig. 6 and the magnetic parameters are tabulated in Table 2. The magnetization of ferrites is affected by the temperature. The M-H loops of all samples annealed at different temperatures 400 °C to 700 °C are showing the same trend; i.e., the overall magnetic behavior of the samples is improved with an increase in annealing temperature. The low magnetization is indicating the antiferromagnetic ordering, i.e., hematite, the indication of which is also given in the XRD pattern. This may be attributed to the small quantity of ferrite formation. The samples did not attain the higher magnetization values due to the applied field limitation; usually, the magnetization

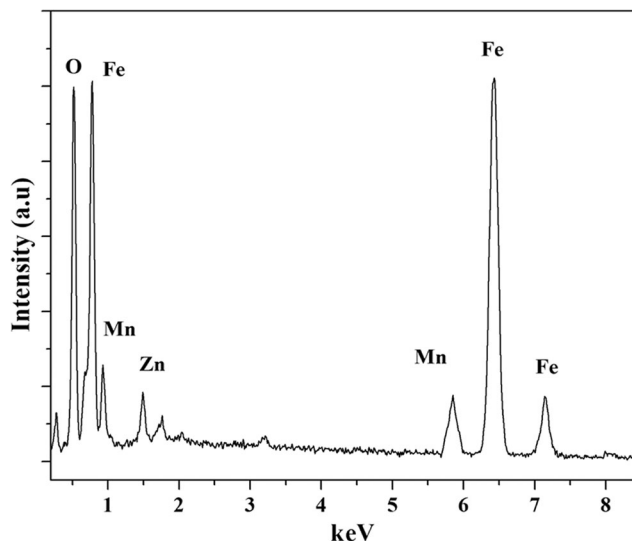


Fig. 5 EDX spectrum of Mn-Zn ferrites nanoparticles showing the required contents

increases with the temperature and attains the maximum value for the field higher than 12,000 Oe. However, in our results, we observe an overall increase in saturation magnetization with the increase in annealing temperature that is due to the better alignment of magnetic domains owing to the release in the stress among the grains and better ordering of directional atomic pairs [27–29].

Figure 7 shows the change in coercivity and squareness with the increase in annealing temperature illustrating the increase in both the magnetic parameters to a maximum value and then decrease. Similar to the increase in the saturation magnetization values, the increase in coercivity values is also due to the removal of impurities and stress relief among the grains as this leads to the better alignment of grain and ultimately the improved manifestation of magnetic domains after receiving the external magnetic field. Furthermore, the sudden decrease of these two magnetic parameters at higher temperatures as shown in the figure could have a few possible

Fig. 4 SEM images of as-synthesized $Mn_{0.5}Zn_{0.5}Fe_2O_4$ nanoparticles

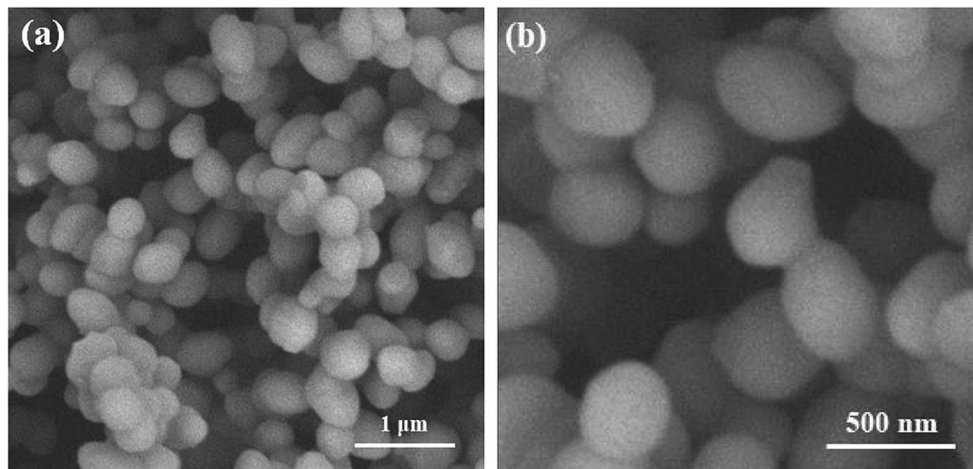


Table 2 Variation in different magnetic parameters and crystallite size of $\text{Mn}_{0.5}\text{Zn}_{0.5}\text{Fe}_2\text{O}_4$ nanoparticles annealed at different temperatures

Sr. no.	Samples	M_s (emu/g) $\times 10^{-3}$	M_r (emu/g) $\times 10^{-6}$	$\text{SQ} = M_r/M_s$	H_c (Oe)	Crystallite size (nm)
1	As synthesized	26.51	31.02	0.0012	13.815	14.47
2	400 °C	42.83	662.45	0.015	143.28	18.64
3	500 °C	28.04	563.01	0.020	192.94	20.64
4	600 °C	61.20	704.27	0.011	84.343	22.49
5	700 °C	65.58	797.80	0.012	48.723	24.69

reasons. One of the possible reasons is that the melting points of several materials when they are in the nanometer range are considerably smaller than their counter bulk parts. So this could be one of the reasons that up to some extent, there can be melting effects leading to the formation of non-magnetic oxide causing the reduction in coercivity and squareness values. Another possible reason is that with the increase in annealing temperature, there is a possibility of the formation of regions having antiferromagnetic orderings and this causes a loss of free ferromagnetic iron atom and again causing a decrease in coercivity value. Ions have their own site preference energy for the occupancy of specific site. It is unlikely for the Mn^{2+} ions to occupy all octahedral sites; consequently, no B-B or $\text{Fe}^{3+}\text{-O-Fe}^{3+}$ magnetic interaction is possible in the MZF [20, 30, 31]. On the other hand, it is reported that a part of total Mn^{2+} can occupy the octahedral site that is why it is not surprising that MZF shows lower magnetization at higher concentration of zinc since zinc does not take part in the magnetic properties, filled d orbitals, or zero magnetic moments [18, 20].

After dissolving in distilled water, the UV-visible absorbance spectrum of $\text{Mn}_{0.5}\text{Zn}_{0.5}\text{Fe}_2\text{O}_4$ nanoparticles has been recorded in the range 200–800 nm wavelength as shown in Fig. 8. The measurements have been done in a usual way of

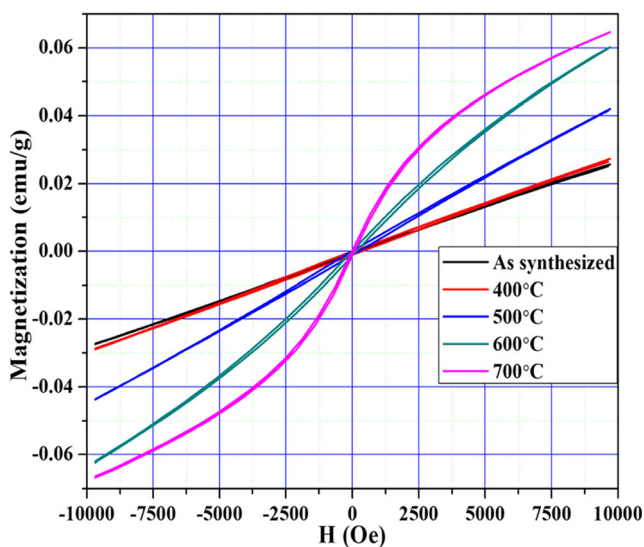
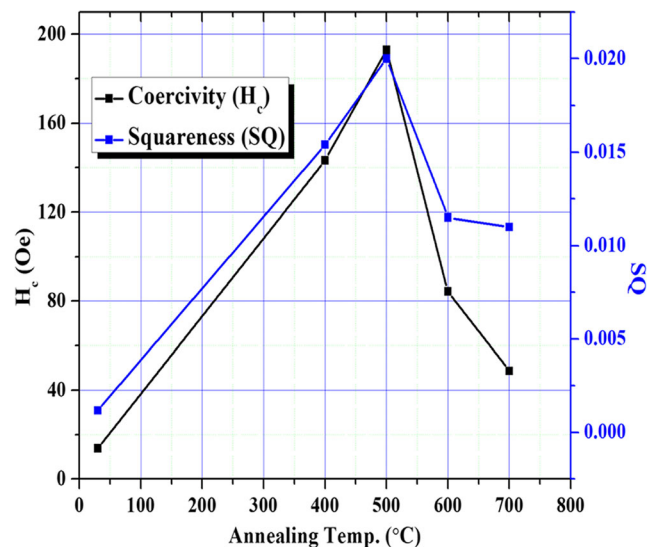
transmittance mode in which basically the ratio of transmitted and incident radiation is recorded. The next useful step is to take the negative logarithm of transmittance that gives the absorbance against the wavelength range as shown in Fig. 8. In transition metals, the 3d and 4d orbitals are responsible for the absorption mechanism. The maximum absorbance is observed at 380 nm and the optical absorbance coefficient is calculated using the following relation [20].

$$\alpha = 2.303 \frac{A}{t}$$

where α is the optical absorption coefficient, A is the absorbance, can be calculated from the absorbance spectrum corresponding to the wavelength, and t is the thickness of the sample, usually taken as 1 cm. The emission wavelength from a semiconducting material is related to the band gap or material constant. The band gap E_g is calculated using the relation [32].

$$\alpha h\nu = A(h\nu - E_g)^2$$

In the above relation, the value of n determines the allowed direct and indirect band gap. The value of n is 0.5 in case of allowed direct transition. Figure 9 shows the Tauc plot or plot between $(\alpha h\nu)^2$ and $h\nu$, by extending the linear part of the

**Fig. 6** Magnetic hysteresis curves for $\text{Mn}_{0.5}\text{Zn}_{0.5}\text{Fe}_2\text{O}_4$ nano-powder annealed at different temperatures**Fig. 7** Variation in coercivity and squareness with the increase in annealing temperature

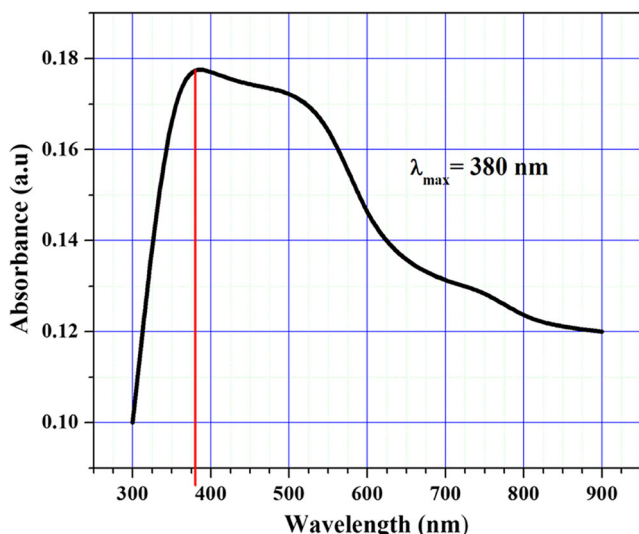


Fig. 8 UV-visible absorbance spectrum of $Mn_{0.5}Zn_{0.5}Fe_2O_4$ ferrite nanoparticles

plot to the energy axis gives the optical band gap. The calculated value of the optical band gap for the $Mn_{0.5}Zn_{0.5}Fe_2O_4$ is 3.05 eV. The estimated value of the band gap is in accordance with the reported literature. The literature reported the band gap energies of Mn-Zn ferrites in the range of 2.62 to 3.09 that have different size, metal substitution ratio, geometry, and synthesis method [31].

The larger band gap is attributed to the quantum confinement effect. The implication of the quantum confinement effect is the allowed transition between the discrete energy levels of the electron. The most important implication is the $1/a^2$ dependence or simply if you change the size of the quantum well (i.e., particle size), the band gap will tune-up. The reduction in the size of the particle made the density of states becomes more quantized and the band gap shifts to higher energy; the material spectrum shows a blue shift. The high

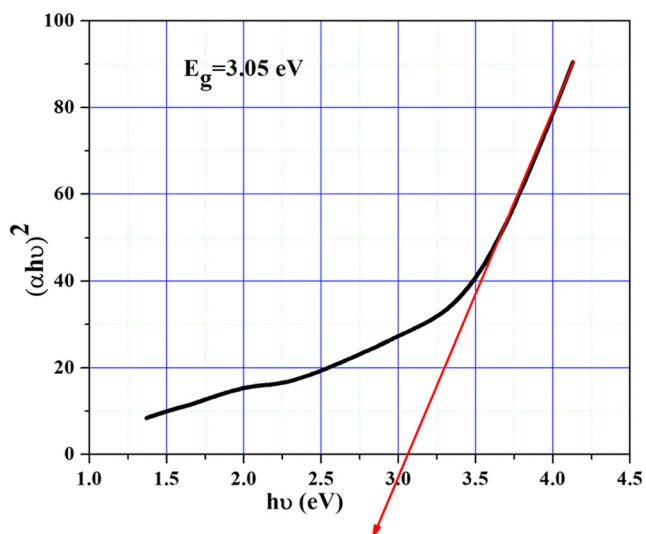


Fig. 9 Variation of $(\alpha h\nu)^2$ with photon energy ($h\nu$)

blue shift may be attributed to the high concentration of metal substitution. The size, synthesis method, and metal substitution are the potential parameters that affect the optical band gap [33–35].

4 Conclusion

The nanocrystalline $Mn_{0.5}Zn_{0.5}Fe_2O_4$ ferrites in powder form have been prepared by the co-precipitation method by varying temperature ranges from 400 to 700 °C. Keeping in mind the heat treatment, the ferrite samples have been investigated for structural, magnetic, and optical behavior by employing XRD, VSM, and UV-Vis spectrophotometer respectively. The crystallite size increases from 14 to 24 nm with the annealing temperature due to Ostwald ripening mechanism which let the smaller particles to get dissolve into the bigger grains and this is basically one of the attributions of the grain growth process. XRD results reveal that crystallinity increases with temperature as shown with the sharper peaks. At a temperature lower than 600 °C, the hematite phase with a poor magnetic response is formed which is started to dissolve or convert into the ferrite phase at a temperature higher than 600 °C. SEM micrographs reveal that morphology is porous and agglomerated but homogeneity increases with temperature. The UV-Vis spectroscopy study shows the intense absorption peak at 380 nm and the value of the optical band gap calculated with the Tauc plot is 3.05 eV. This might be attributed to the high concentration of transition metal and quantum confinement effect. VSM results report the increase in saturation magnetization with annealing temperature owing to decreased impurity contents which in turn provides better alignment of magnetic domains. This is confirmed through the graph between squareness ratio and temperature too. The sample annealed at 700 °C shows fine crystalline structure, homogenous particle size distribution, larger saturation magnetization value of 65.58×10^{-3} emu/g, and lower coercivity value of 48.723 Oe. This could be attributed to the enhancement in phase purity, crystallinity, size distribution, and crystallite size.

Funding This work is supported by the Higher Education Commission of Pakistan under Start up Research Grant Program (SRGP) No. 21-1096/SRGP/R&D/HEC/2016.

References

- Xu, Z., Fan, J., Liu, T., Han, Y., Zhang, H.: J. Alloys and Compounds. **814**, 152307 (2020)
- Ren, J., Zhang, Z., Ma, X., Zhong, Y., Zhang, J., Ren, Z., Liu, Y.: J. Magn. Mater. **495**, 165832 (2020)
- Malles, S., Srinivas, V., Vasundhara, M., Kim, K.H.: Phys. B Condens. Matter. **582**, 411963 (2020)

4. Prado, L.E., Hernández, D.A., Robles, J.M., Bocardo, J.C., Sánchez, J., Rdz, P.Y., Terán, R.A., López, G.F.: *J. Magn. Magn. Mater.* **427**, 230–234 (2017)
5. Tangcharoen, T., Ruangphanit, A., Pecharapa, W.: *Ceram. Int.* **39**, S239–S243 (2013)
6. Bahadur, D.: *J. Bull. Mater. Sci.* **15**, 431–439 (1992)
7. Al-Hada, N.M., Kamari, H.M., Shaari, A.H., Saion, E.: *Results in Physics.* **12**, 1821–1825 (2019)
8. Bersweiler, M., Bender, P., Vivas, L.G., Albino, M., Petrecca, M., Mühlbauer, S., Erokhin, S., Berkov, D., Sangregorio, C., Michels, A.: *Phys. Rev. B.* **100**, 144434 (2019)
9. Nekvapil, F., Bunge, A., Radu, T., Pinzaru, S.C., Turcu, R.: *J. Raman Spectrosc.* **51**, 959–968 (2020)
10. Alla, S.K., Kollu, P., Meena, S.S., Poswal, H.K., Mandal, R.K., Prasad, N.K.: *Mater. Res. Bull.* **104**, 65–71 (2018)
11. Tsay, C.Y., Chiu, Y.C., Tseng, Y.K.: *Phys. B Condens Matter.* **570**, 29–34 (2019)
12. Hu, X., Liu, B., Liu, J., Qin, J., Zhao, W., Lam, K.H.: *J. Photochem. Photobiol. A Chem.* **382**, 111903 (2019)
13. Tatarchuk, T., Naushad, M., Tomaszewska, J., Kosobucki, P., Myslin, M., Vasylyeva, H., Ścigalski, P.: *Environ. Sci. Pollut. Res.* **27**, 26681–26693 (2020)
14. Tatarchuk, T., Shyichuk, A., Trawczyńska, I., Yaremiy, I., Pędziwiatr, A.T., Kurzydło, P., Bogacz, B.F., Gargul, R.: *Ceram. Int.* **46**, 27517 (2020). <https://doi.org/10.1016/j.ceramint.2020.07.243>
15. Shebl, A., Hassan, A.A., Salama, D.M., Abd El-Aziz, M.E., Abd El Wahed, M.S.A.: *Heliyon.* **6**, e03596 (2020)
16. Sharma, A., Batoo, K.M., Raslan, E.H., Kumar, G.: *J. Mater. Sci. Mater. Electron.* **31**, 16959 (2020). <https://doi.org/10.1007/s10854-020-04252-3>
17. Goncalves, E.S., Cocca, L.H.Z., Araujo, W.W.R., Parekh, K., Oliveira, C.L.P., Siqueira, J.P., Mendonca, C.R., Boni, L.D., Neto, A.M.F., Phys, J.: *Chem. C.* **124**, 6784–6795 (2020)
18. Rashad, M.M., Nasr, M.I.: *J. Electron. Mater.* **8**, 325–239 (2012)
19. Hu, P., Yang, H.B., Wang, H.: *J. Magn. Magn. Mater.* **322**, 173–177 (2010)
20. Aggarwal, N., Narang, S.B.: *J. Magn. Magn. Mater.* **513**, 167052 (2010)
21. Rath, C., Anand, S., Das, R.P.: *J. Appl. Phys.* **91**, 2211–2215 (2002)
22. Xuan, Y., Li, Q., Yang, G.: *J. Magn. Magn. Mater.* **312**, 464–469 (2007)
23. Meng, Y.Y., Liu, Z.W., Dai, H.C., Powder, J.: *Technology.* **229**, 270 (2012)
24. Patil, R.P., Jadhav, B.V., Hankare, P.P.: *Results in Physics.* **3**, 214 (2013)
25. Li, F.S., Wang, L., Williams, G.: *J. Magn. Magn. Mater.* **268**, 332–339 (2004)
26. Mirchekari, G.R., Daei, S.S., Mohseni, H., *Advanced Material, J.: Research.* **409**, 520–525 (2012)
27. Mallesh, S., Srinivas, V.: *J. Magn. Magn. Mater.* **475**, 290–303 (2019)
28. Li, M., Liu, X., Xu, T., Nie, Y., Li, H., Zhang, C.: *J. Magn. Magn. Mater.* **439**, 228–235 (2017)
29. Shamaila, S., Sharif, R., Chen, J.Y., Liu, H.R., Han, X.F.: *J. Magn. Magn. Mater.* **321**, 3984 (2009)
30. Z. Huanque, H. Fei, Z. Xuelin, S. Qiangqiang, P. Huifen, W. Xin, J. *Magn. Magn. Mater.*, 2017, 439, 245–25-0
31. Jalaiah, K., Babu, K.V.: *J. Magn. Magn. Mater.* **423**, 275–280 (2017)
32. Bhongale, S.R., Ingawale, H.R., Shinde, T.J., Pubby, K., Narang, S.B., Vasambekar, P.N.: *J. Magn. Magn. Mater.* **441**, 475–481 (2017)
33. Baykal, A., Guner, S., Demir, A.: *J. Alloys and Compounds.* **619**, 5–11 (2015)
34. Alkhtaby, L.A., Husain, S., Khan, W.: *Asian J. Chem.* **23**, 5605–5607 (2011)
35. Demir, A., Guner, S., Bakis, Y., Esir, S., Baykal, A.: *J. Inorg. Organomet. Polym.* **24**, 729–736 (2014)

Publisher's note Springer Nature remains neutral with regard to jurisdictional claims in published maps and institutional affiliations.